Check for updates

Research Article Vol. 32, No. 10 / 6 May 2024 / Optics Express 17704

Optics EXPRESS

Process and optical modeling of black silicon

Guillermo Sanchez-Plaza[1,2,4,*] **and Alfonso Urquia**[3,5]

[1] *Nanophotonics Technology Center, Universitat Politècnica de València (NTC-UPV), Camino de Vera, Building 8F, 46022 Valencia, Spain*
[2] *Researcher PhD Candidate, Escuela Internacional de Doctorado, UNED, Spain*
[3] *Departamento de Informática y Automática, Universidad Nacional de Educación a Distancia (UNED), Juan del Rosal 16, 28040 Madrid, Spain*
[4] *gsanchez732@alumno.uned.es*
[5] *aurquia@dia.uned.es*
[*] *gsanchez@ntc.upv.es*

Abstract: Black silicon is relevant for the photovoltaic industry when searching for low-reflectance, low-defect front surface, which is the goal of this work. We have fabricated samples using reactive ion etching (RIE) plus chemical etching for the smoothing, characterized them, and built modeling tools capable of reproducing the resulting geometric features, based on the process parameters. Reflectance is simulated using a proprietary rigorous coupled wave analysis (RCWA)-based tool, and compared with the experimental results. A good matching was achieved using a simple unit cell, and a better agreement when using a 0.5 square microns sample. Finally, an optimum trade-off between low reflectance and low thickness has been achieved.

© 2024 Optica Publishing Group under the terms of the Optica Open Access Publishing Agreement

1. Introduction

The photovoltaic industry learning rate has been 20.2% for the last 46 years [1]. Part is due to cost reduction and part to efficiency improvements. Concerning the later, light trapping is one of the most important design features for solar cells, as it relates to the quantity of captured photons for energy conversion [2–4]. Light trapping was originally achieved by texturing the surface of the wafers with random pyramids, which became the industry standard since the beginning [5] for crystalline silicon solar cells. In parallel, for multi-crystalline silicon material, isotropic microtexturing has been used since the different orientation of the crystals prevents the formation of pyramids [6,7]. But the adoption of diamond wire sawing for wafer slicing [8] reduced the microtexturing, and required the introduction of additives in the chemical baths [9] in order of recovering the low reflectances achieved so far [10].

Nanotexturing of the surface can achieve near-zero reflectance [11], and is then attractive to even high efficiency mono-Si solar cells [2,12,13]. Metal catalyst chemical etching (MCCE) is consolidating as the preferred texturing method for commercial solar cells [14]. In contrast with MCCE, Reactive Ion Etching (RIE) fabricated black silicon achieves near zero broadband reflectance with excellent angular performance, resulting in cells achieving world record results [15,16], and has the potential of overcoming MCCE [17].

The black silicon texture presented in this article is based on RIE. But the surface resulting after RIE is too porous and challenging to use directly in the solar cell, especially for the emitter formation [18] and surface passivation [19]. Therefore, the wafer undergoes a smoothing process, which decreases the porosity whilst maintaining a low reflectivity. This is indeed our goal: understanding how the smoothing process affects the optical response of the samples, so we can define an optimum target for the nanotextured geometry. Besides, we aim at helping the industry in designing the process parameters capable of achieving such geometry, by providing useful modeling and simulation tools.

In order of achieving this goal, we need to understand the initial geometry of the textured surface produced by the RIE, and how the chemical smoothing process affects such geometry; find

#516245 https://doi.org/10.1364/OE.516245
Journal © 2024 Received 18 Dec 2023; revised 16 Apr 2024; accepted 17 Apr 2024; published 30 Apr 2024

Optics EXPRESS

a way of defining mathematically such geometries; and finally understand how all this translates into the optical response of the samples. Therefore, we need a model capable of defining the geometry of the textured layer of the samples after RIE, a model able to reproduce the effect of the chemical smoothing process on such texture, and an optical model reproducing the reflectance of the resulting samples after each process step. These models are discussed in this article. It is well known that an anti-reflection coating layer on top of the nanotextured surface can further reduce the reflectance. Such layer is normally part of the passivation process, but his effect on the reflectance has not been studied in the present work.

Simulations are useful for the understanding of how the geometry of a nanotextured surface affects its optical response. Reactive ion etching and isotropic chemical etching, the processes used in this study to create the black silicon, are unstable processes that are difficult to control and reproduce, because small variations in temperature and other parameters have a significant effect of the nanopore size and shape. Additionally, experimental samples contain a lot of variability, while in contrast, simulations are fully reproducible, with nanopore size and shape that can be completely tailored for research purposes.

The article is structured as follows. After the introduction, we describe the experimental part, including the two fabrication processes (RIE and smoothing), followed by the physical and optical characterization procedures we have used. Then we describe the geometric model, and how we include the two fabrication processes within the model, and the characteristic geometry arising after the overlapping of two or more holes. Right after this, we explain the two modeling tools developed for this work: the cellular automaton for the smoothing process and the RCWA-based tool for the optical modeling. Finally, we discuss the most relevant results and conclusions.

2. Sample preparation and characterization

To manufacture the samples, a two-step sequence was applied on 6-inch initially polished 10-20 ohm/cm P/B doped <100> mono-crystalline silicon wafers: RIE texturing, and smoothing.

2.1. RIE texturing

We have created a recipe based on a sulphur hexafluoride-oxygen ($SF_6 + O_2$) mixture gas, on an inductively coupled plasma (ICP) RIE etch system model STS AOE multiplex plasma etcher. We have adjusted the process pressure at a high value (50 mT) to favour the positive ions collisions and thus reduce the bias voltage. The 13.56 MHz generator connected to the chuck was adjusted to a minimum value of 15 W also to get a very low bias voltage. The ICP source generator was fixed at an average value of 1000 W, and the chuck was cooled at a temperature of 0 °C, low enough to allow the creation of a passivation layer of SO_xF_y made by the by-products of the etching species SF_6 (mainly sulphur tetrafluoride (SF_4)) and the oxygen radicals. The last part of the process development consists of adjusting the gas ratio between the O_2 and the F_6 to get an etching/passivation competition to create the black silicon. The O_2:SF_6 ratio was 2:1. The etch rate is very slow when the black silicon is created, and we had to etch at least 15 min to get the black silicon (structures 500 nm high).

2.2. Smoothing

The smoothing process is achieved using a mixture of hydrofluoric acid (HF), nitric acid (HNO_3) and acetic acid (CH_3-COOH), where the proportions of the mixture have been adjusted to obtain speeds of attack on the order of 4 nm/sec on black silicon samples. This process has been carried out at room temperature during 30, 60, and 120 seconds, followed by a rinse cycle with DI water and drying by centrifugation in a nitrogen atmosphere.

Optics EXPRESS

2.3. Physical characterization

Experimental samples have been characterized to obtain their geometric characteristics. We have used a high-resolution HITACHI S-2400 field emission scanning electron microscope (FE-SEM), and the samples have been prepared with usual cleavage techniques and cleaning. Samples have not been chemically decorated, neither coated with any layer.

Our geometric model of the nanotextured surface considers the number of holes per unit area; and a function that describes the hole shape and size. We simplify things by assuming that the air holes are solids of revolution obtained by rotating the curve

$$z = H \cdot \left(\frac{r}{R}\right)^n \tag{1}$$

around axes in the z-direction, where H, R and n are geometric parameters whose values are fitted from SEM images; and z and r are the height and radius cylindrical coordinates. The hole density is 71.5 holes/μm^2, estimated from SEM top-view images (Fig. 1) by counting the number of holes and dividing it by the total area. The value of R is taken as half the average distance D between the centers of adjacent holes, measured from SEM top-view images, which is $D = 167$ nm in our samples, and consequently $R = D/2 = 83.5$ nm. The corresponding values of H and n are fitted from SEM cross-section images (Fig. 2), and summarized in Table 1.

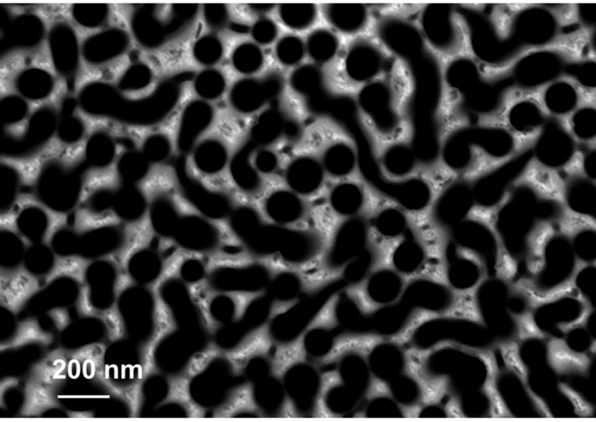

Fig. 1. Example of the SEM top-view images taken from RIE samples and used for estimating the density of the holes per surface unit and the R parameter.

Table 1. Geometrical values of the silicon nanostructures respect to smoothing time.

Smoothing time (secs.)	Max. peak-to-valley height (nm)	H (nm)	R (nm)	n
0 (RIE)	716	500	83.5	2.5
30	528	480	83.5	2.8
60	360	320	83.5	3.0
120	230	141	83.5	3.8

2.4. Optical characterization

Measurement setup is depicted in Fig. 3(a), and uses a spectrometer from Instrument Systems, model CAS 140 CT, for the UV-visible-IR range, with a halogen lamp, and an integrated sphere that has a 150 mm diameter and a 20 mm diameter sample aperture. The system is mounted in the d/8° configuration and the detector port is equipped with a collimating tube and a lens system

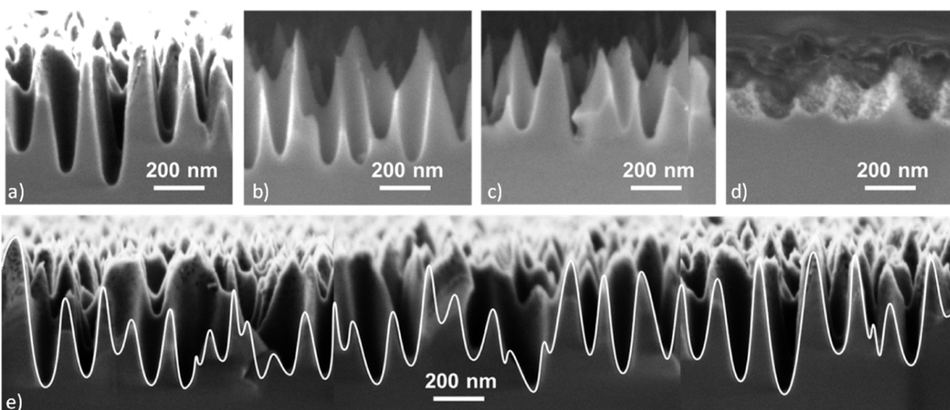

Fig. 2. SEM cross-section images of the samples after: a) RIE; b), c) and d) 30, 60 and 120 seconds of chemical smoothing respectively. e) Image obtained by overlapping several consecutive SEM cross-section images from a RIE sample, and highlighting the cross-section profile of the interface between the nanotextured surface and the air.

for coupling the light into the fiber. The sphere contains one port for the input light, located at 90° with respect to the sample, and one port for collecting the light located at 8° with respect to the sample vertical. The system is equipped with a screen that prevents the input light to impact directly to the sample.

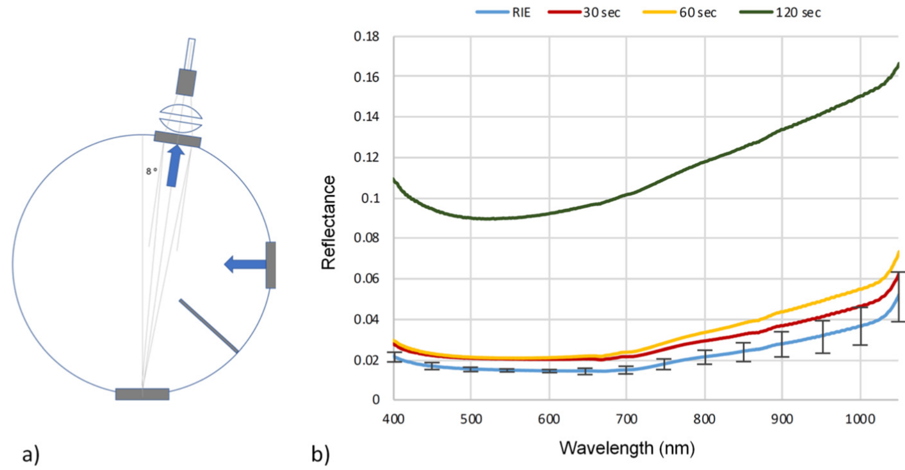

Fig. 3. a) Experimental setup; and b) measured reflectance of samples.

Reflectance was measured after RIE and then the wafer was cut into 4×4 cm pieces. 3 samples were chemically etched 30, 60, and 120 seconds, and reflectance measured before and after. Measurements using this set-up are plotted in Fig. 3(b). The repeatability (measured as 3 times the standard deviation of the 4 samples) of the reflectance after RIE ranged from 0.002 at 400 nm wavelength to 0.010 at 1000 nm (error bars are depicted in Fig. 3(b)). The photometric transmission measurement accuracy of the instrument is ±0.5% T [20].

3. Geometric modeling

The geometric model is needed for feeding the optical model with values that are representative of the main features of the experimental sample's geometry. The output of the geometric model will be the z values of the textured surface, for a dense mesh (1 nm step) of x and y points.

3.1. RIE process

RIE can be seen as the combination of two simultaneous processes competing between them at the same time: an almost vertical etching of the silicon and the deposition of a polymer layer over the surface. If the deposition rate is higher than the etching rate, the silicon surface will be completely covered by a polymer layer. If, on the contrary, the etching rate is much higher than the deposition rate, the whole surface will be etched away.

Obtaining black silicon material [21] implies finding a process regime where the deposition and etching rates of the polymer are similar. In that situation, the result will be of areas covered of polymer, and areas or points where the etch has started. Once a hole starts in the silicon surface, the polymer deposition creates a sidewall layer that becomes more and more difficult to remove as the depth of the hole increases. As a result, the hole will move quickly downward and slowly sideways, resulting on the cross-section profiles of parabolic shape observed in Fig. 2(a). Moreover, as the hole widens, the overlapping with the surrounding holes creates a characteristic surface profile.

3.2. Overlapping effect

The overlapping of three identical holes equally spaced produces a needle shaped column, whose width widens progressively downwards (Fig. 4). We can extend the model to a hexagonal unit cell (red rectangle in left side of Fig. 5(a)), and represent it as a three-dimensional plot (right side of Fig. 5(a)), where the center hole is surrounded by 6 needle shaped columns, each one located at a point where three holes intersect.

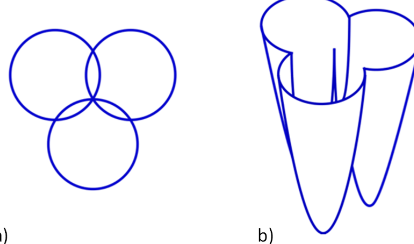

Fig. 4. Three holes intercepting in one point: a) top view; and b) three-dimensional representation.

In this situation, where all the holes overlap each other, the resulting surface can be seen as a set of holes with a set of needles at the intersection points. Both the holes and the needles constitute the elements that will determine the optical properties of the samples. On the other hand, the models documented in the literature thus far, up to the best of our knowledge, are either using cones arising from the surface and rising [22–30], or holes that progresses downwards [31,32]. In contrast, and this is a novelty of this study, our model combines both elements, where the holes overlap each other, producing a sort of needles at the intersection points. Both the holes and the needles constitute the elements that will determine the optical properties of the samples.

As we can see from the right side of Fig. 5(a), the height of the needles (measured from the lowest point of the intersection of the holes, up to the surface) is only a 30% of the total height of the structure. Based on our calculations, if we reduce the size of the holes (both in depth

Optics EXPRESS

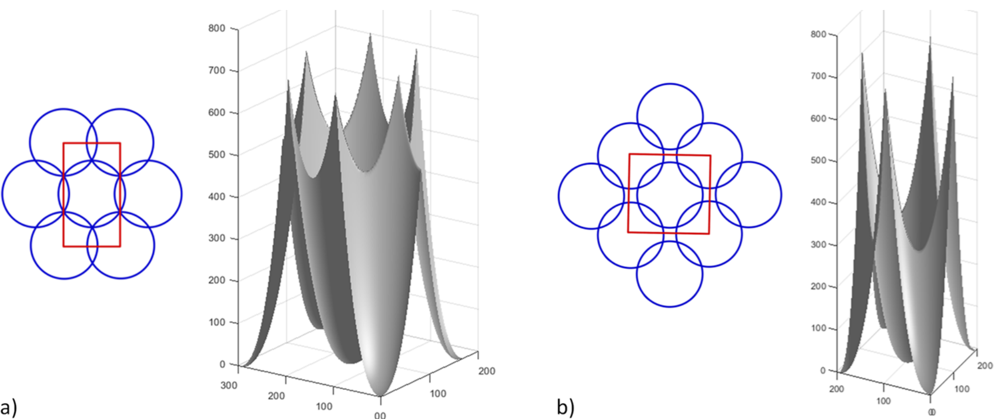

Fig. 5. Top-view representation of holes forming a) hexagonal and b) square lattices, with unit cells in red, and three-dimensional representation of unit cells.

and width), the total structure height and the needles height changes, but the 30% ratio remains unchanged. Likewise, if we increase or reduce the spacing between the holes, the 30% ratio becomes equally unchanged, and therefore, we can conclude that such ratio between the needles height and the total height is an intrinsic property of the hexagonal type of structure.

On the contrary, if we move from a hexagonal type of structure to a square type of structure (see the left side of Fig. 5(b)), such ratio changes, and the height of the needles becomes a 60% of the total height of the structure, as we can observe in the right side of Fig. 5(b). The importance of the ratio between the height of the needles and the total height, and its influence on the reflectance will be discussed further on in Section 6.1.

3.3. *Smoothing chemical etching*

The smoothing process is isotropic, i.e., etches equally in all directions. In order of reproducing the effect of the isotropic etch, we can modify the z values of the hexagonal unit cell, translating them perpendicularly a distance equal to the value etched at each point of the surface, where the translating vector will be perpendicular to the original surface at each point. Once we have done this for each of the holes, we make again the interception of the seven functions. Additionally, we have to consider that the interception of the holes will also be etched, so we have to add another modification of the z coordinates, this time in the vertical direction downwards, to all the intersection areas.

4. Modeling the chemical smoothing using cellular automaton

Simulating the isotropic etch process of large nanotextured surfaces using the geometric model described in Section 3.3 is unpractical, so we have developed a three-dimensional cellular automaton (CA). The modeled system includes the nanotextured surface region, described as a silicon background with inclusions occupied by chemical reactants during the smoothing process; the superstrate, which is filled of chemical reactants during the smoothing process; and the silicon substrate below the nanotextured surface region. The system is modeled using an homogeneous CA (i.e., neighborhoods, state transition rules and topology are the same for all cells). Superstrate, nanotextured surface, and substrate are three-dimensional rectangular volumes. Space is discretized into a three-dimensional grid composed of identical cubic cells, with faces parallel to the coordinate planes. The edge length of the cubic cell is $d = 1$ nm.

The CA boundary conditions are as follows. The system periodicity in the x- and y-directions is described by imposing periodic boundary conditions to the x- and y-directions of the cell space, i.e., the space is wrapped around the x-axis and around the y-axis. Adiabatic boundary conditions (i.e., the cell value is duplicated in an extra virtual neighbor) are imposed in the z-direction.

Each cell has a discrete state. The cell state is described by an integer number in the set $\{0, 1, 2\}$, which indicates that the cell contains only reacting chemicals (0 state); only silicon (2 state); or both reacting chemicals, and silicon (1 state).

The neighborhood of a cell is composed of the six cells adjoining its six faces (von Neumann neighborhood). Cell interactions with its six neighbor cells take place through the six faces of the cell. Each face is shared by two neighbor cells. A face is said to be "exposed" if one of the cells that shares this face is in the 0 state, and the other is not in the 0 state. A cell is said to have "parallel exposed faces" if two faces parallel to the same coordinate plane are exposed. At discrete times (periodic clock ticks), the state of the cells is simultaneously updated as determined by the transition rule in Table 2. From this rule and the cubic cell size ($d = 1$ nm), the etch rate to a flat horizontal Si surface is 0.5 nm per tick. This allows to calculate the relationship between the CA ticks and the "wall clock" time.

Table 2. Transition rule of the cellular automaton.

Actual state	Exposed faces?	Parallel exposed faces?	New state
0	don't care	don't care	0
1	no	no	1
1	at least one	don't care	0
2	no	no	2
2	at least one	no	1
2	at least one	yes	0

The nanotextured surface prior to the chemical smoothing, $z = f(x, y)$, is specified by a z-value matrix (i.e., a matrix element is the z-value of the surface at the xy-coordinates represented by the column-row index of the element), which is used to initialize the CA as described next. CA cells whose geometric center is below the surface are assumed to contain only silicon, and therefore their initial state is 2. The rest of cells are initially in the 0 state, as they contain only reacting chemicals. The initial thickness of silicon under the nanotextured surface is set to an arbitrary value large enough to not be completely etched during the smoothing process.

5. Reflectance simulation using RCWA

A simulation tool named Argia has been employed to compute the reflectance of the nanotextured silicon surface, modeled as a three-dimensional diffraction structure periodic in x- and y-directions. Argia is an implementation, developed by the authors of the rigorous coupled wave analysis (RCWA) method in MATLAB. Chapter 6 of [33] and Chapter 2 of [34] provide clear and detailed descriptions of the standard RCWA method implemented in Argia.

Argia allows to calculate the diffraction efficiencies of a grating illuminated from the top by a monochromatic plane wave, incident with θ and ϕ angles, with TE or TM polarization. The θ angle is the incidence angle defined with respect to the surface normal, and ϕ is the angle relative to the x-axis of the line defined by the intersection of the incidence plane and the xy-plane.

Argia employs the "conventional" truncation scheme of the spatial harmonics [33] (i.e., the k-space region defined by the indices of the spatial harmonics retained in the expansion is rectangular). To avoid slow convergence for TM polarization, the series expansion of the electric displacement is calculated by Argia applying the Li's factorization rules for two-dimensional gratings [34,35].

Optics EXPRESS

The grating is discretized in parallel layers perpendicular to the z direction, and the eigenmodes are computed for each layer. The boundary conditions for the fields inside the grating layers, and the reflected and transmitted fields, are solved in Argia using the enhanced transmittance matrix (ETM) method [33,36].

Each layer is homogeneous in the z-direction, and is defined by its texture and thickness. Two types of textures are supported in Argia: uniform textures, composed of a homogeneous material; and binary textures, composed of an homogeneous material (background) with inclusions of another homogeneous material (motif). Argia supports a variety of materials, taking automatically into account the dependence of the refractive index of these materials with the incident wavelength. The gratings simulated in the presented study are composed of homogeneous and binary textures of air, and monocrystalline silicon.

Gratings can be defined in Argia by specifying the texture and thickness of each layer. The layer texture can be specified in Argia in any of the three following ways: describing the motif as a set of overlapping and/or non-overlapping rectangles with sides parallel to the x- and y-directions; describing the motif as a set of overlapping and/or non-overlapping circles; and by means of a binary matrix whose 0/1 elements indicate whether the background (0) or the motif (1) material is present in the x-y position defined by the corresponding column-row indexes.

Every circular inclusion is automatically translated by Argia into a set of non-overlapping rectangles with sides parallel to the x- and y-directions. The number of rectangles used in this approximation is specified by the user. A similar approach is adopted in other RCWA simulators, e.g. RETICOLO-2D [37].

Argia also allows to specify the grating by providing a matrix representing the nanotextured surface $z = f(x, y)$, where the matrix element is the z-value of the surface at the xy-coordinates represented by the column-row index of the element. The gratings simulated in this article have been defined specifying their interface functions as z-value matrices, with a grid size of 1 nm in the x- and y-coordinates. Argia automatically generates the corresponding layers, each described as a set of non-overlapping rectangles with sides parallel to the x- and y-directions.

The step size of the grating discretization in the z-direction, i.e. the number of layers, can have a significant impact on the simulation accuracy, which can be estimated by repeating the simulation for different discretization schemes. This analysis has been conducted for the presented simulations, being concluded that 4-nm-thick layers provide a valid trade-off (for the gratings and purpose of our study) between accuracy and simulation speed. Another parameter of the RCWA method that affects the result accuracy, and therefore needs to be tuned, is the number of spatial harmonics retained in the calculation. The error introduced by truncating the Fourier series has been estimated performing convergence tests, which have allowed to decide on the number of spatial harmonics to employ in each simulation.

6. Results and discussion

6.1. First optical results of the unit cell

The three-dimensional recreation of the unit cell has been useful for understanding the geometric properties of black silicon, and will be also used to simulate how these geometric properties affect the optical response, which is a novelty of this study. To achieve this, we feed Argia with the matrices representing the nanotextured surfaces $z = f(x, y)$ of the hexagonal unit cell after RIE, and the unit cells obtained from the geometric model for isotropic etch described in Section 3.3. The RIE, and 30, 60 and 120 secs nanotextured surfaces are automatically discretized in the z-direction into 180, 132, 90 and 58 layers, each one 4-nm-thick. Figures 6 and 7 illustrate the grating discretization into layers, and the layer texture definition.

The setup for reflectance simulation is as follows. The substrate under the nanotextured surface is silicon 675 μm thick (the wafer thickness), and air. The superstrate (incident medium) is air. Reflectance is simulated for $\theta = 8°$ and $\phi = 0°$ incidence angles, TE and TM polarizations, and

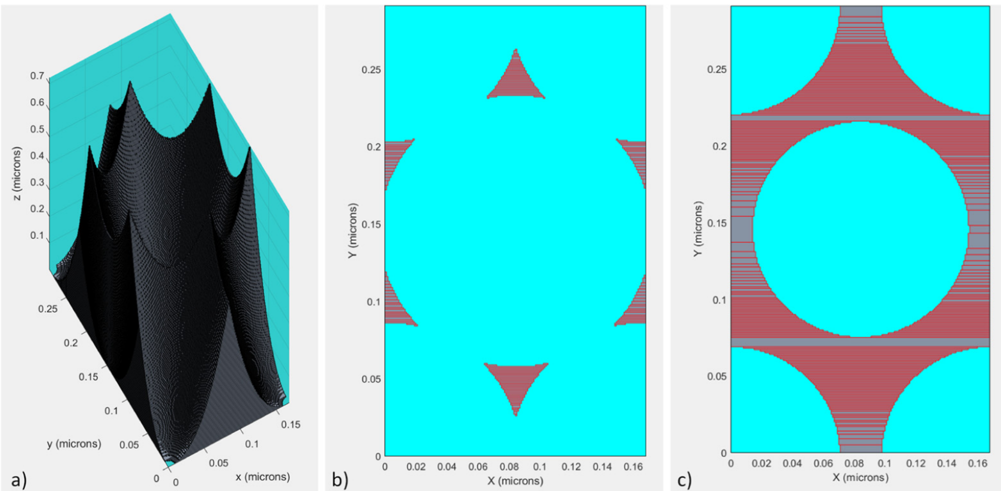

Fig. 6. a) Discretization into 180 layers of the unit hexagonal cell after RIE; and b) and c) layers number 40 and 100, composed of air (background in blue) and silicon (gray rectangles with red border). Layers are 4-nm-thick.

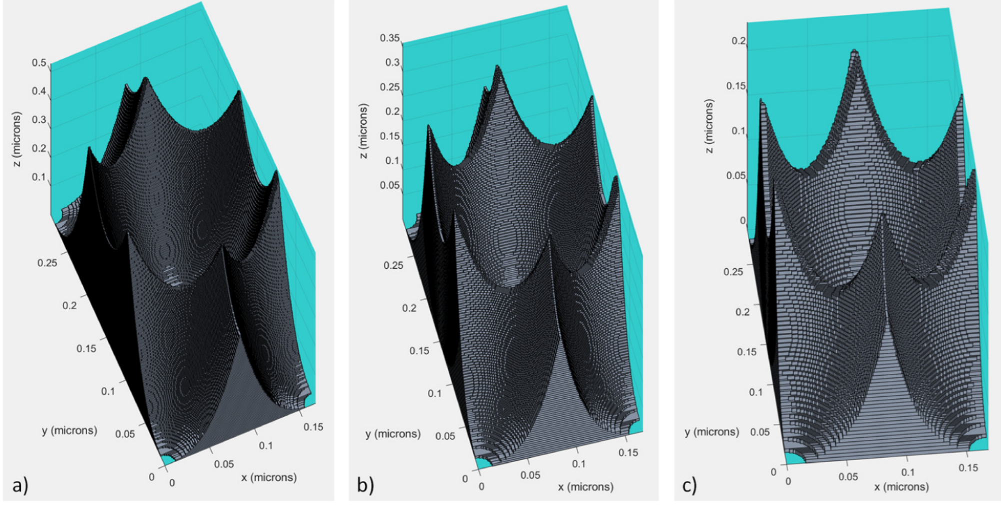

Fig. 7. a), b) and c) Discretization into 132/90/58 layers of gratings obtained simulating 30/60/120 secs of smoothing (geometric model, Section 3.3). Layers are 4-nm-thick.

wavelengths $\lambda = \{400\text{ nm}, 425\text{ nm}, 450\text{ nm}, \ldots, 1050\text{ nm}\}$. As the unit cell periods in the x- and y-directions are $\Lambda_x = D$ and $\Lambda_y = \sqrt{3} \cdot D$, more spatial harmonics are retained along the y-direction than along the x-direction: $nn_1 = \text{round}\left(nn_2 \, / \, \sqrt{3}\right)$. The reflectances obtained for TE and TM polarizations are averaged, for each wavelength. The simulated reflectances are plotted in Fig. 8.

The results reproduce qualitatively the reflectance variations of the smoothing process observed experimentally (Fig. 3(b)). Right after RIE, the reflectance is very low along the whole spectrum, and rises at a low rate first, and increases as the etching time progresses (right side of Fig. 8). The average reflectance values over the whole spectrum are remarkably similar to the ones observed

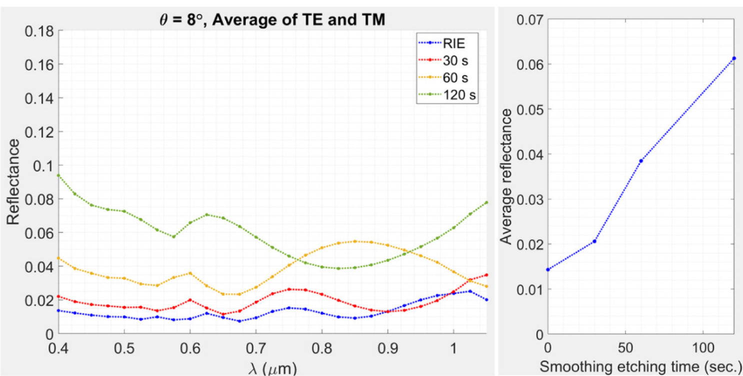

Fig. 8. Simulated reflectances of the hexagonal unit cells.

on the experimental samples (see the optical characterization section), with values below the experimental ones for the RIE, 30 and 120 secs samples, and above for the 60 secs sample.

If instead of using the hexagonal unit cell we use the square unit cell (Fig. 9), we can compare the reflectance of the two types of cells for the RIE case, obtaining the results depicted in Fig. 10. The results are almost identical between the two types of cells for the high part of the spectrum, and slightly different for the lower wavelengths. These findings can be understood in terms of a different transition of the refractive index when comparing the two types of cells. Indeed, several authors [38,39] relate the low reflectance of a nanotextured surface with a gradual transition between the air refractive index and the silicon refractive index. In such model, they differentiate among two different transition areas: from air to the textured layer by one side, and from the textured layer to the bulk silico by the other. The same authors conclude that in order of achieving a nearly zero reflectance surface, both transitions need to be as gradual as possible.

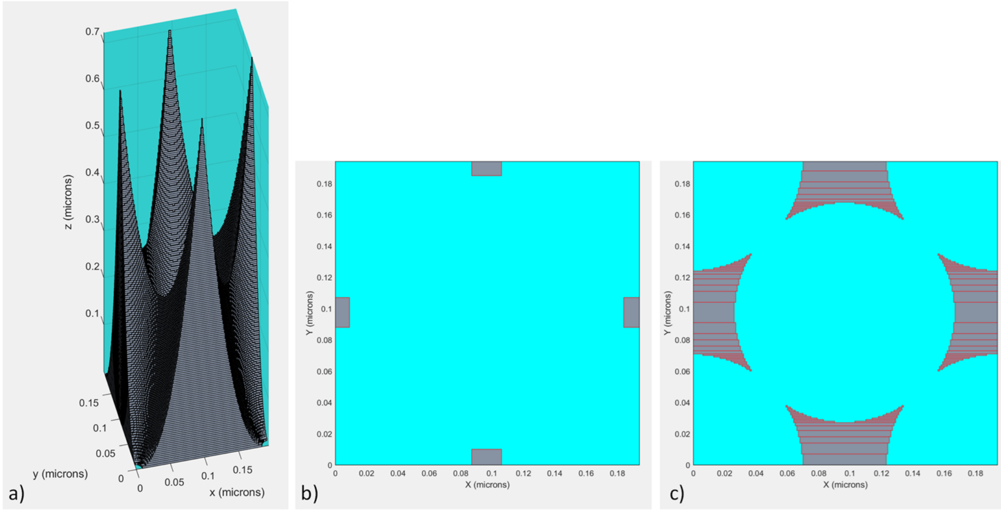

Fig. 9. a) Discretization into 180 layers of the unit square cell after RIE; and b),c) Layers number 40 and 100, composed of air (background in blue) and silicon (gray rectangles with red border). Layers are 4-nm-thick.

In our case, the transition between the air and the structured layer is determined by the height and the number of needles of the structure, whereas the transition between the structured layer

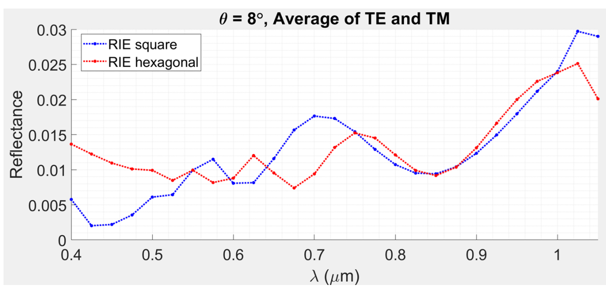

Fig. 10. Reflectance of hexagonal and square unit cells after RIE.

and the bulk substrate is determined by the shape of the bottom of the holes, its depth and the density of holes per unit area. As we reviewed in Section 3.2, in the case of the square cell we have 4 needles per unit cell, representing a 60% of the total height of the structure. On the contrary, in the hexagonal cell we have 6 needles per unit cell, representing the 30% of the total height of the structure. The transition between the air and the structured layer is therefore more gradual in the case of the square cell, which would translate into a lower reflectance. Such effect is apparent at the low part of the spectrum in Fig. 10, since the absorption coefficient of silicon is higher in that part, and the light is absorbed near the surface. As the wavelength increase, silicon becomes more transparent, and the structured layer geometry affects on a more averaged way, which explains why the reflectance curves are almost equally at that part of the spectrum in Fig. 10, since the total height and shape of the holes are the same for the two types of cells.

In summary, the results of the optical modeling of the unit cell are useful, since they reproduce the same trends observed in the experimental samples. Nevertheless, they showed a wavy response whose amplitude increases with the wavelength, which makes difficult to compare the specific reflectance values with the experimental results.

6.2. Simulation of 0.5 μm^2 samples

The idealized representation of the nanotextured surface using a hexagonal unit cell represents approximately the surface texture in the z-direction at the scale of hundredths of nanometers. The simulated reflectance of this model exhibits oscillations (see left side of Fig. 8) that are not observed in the experimental readings (see Fig. 3(b)). In order of reducing such variation of the amplitude of the reflectance spectrum, we can increase the sample area, with a random positioning of the holes, such as we have observed in the experimental samples (Fig. 1). This will increase the geometric variability of the modeled sample, will almost destroy the periodicity of the unit cell and would helpfully reduce the amplitude variation as it has been reported so far. We have chosen a sample size of 0.5 μm^2 with 36 holes. This number of holes reproduces the hole density observed in the experimental samples (i.e., 71.5 holes/μm^2, as described in Section 2.3).

Moreover, we want that our model considers the stochastic nature of the fabrication processes of the experimental samples, and in contrast to earlier research, this method is unique, in such a way that our samples are not identical to a given sample, but statistically representative of the experimental samples analyzed. I.e. that the positions, geometric size and shape of the holes were statistically representative of the experimental samples. In order of achieving this, in our model, we create the holes and arrange them randomly, one at a time, with the only restriction of being far enough to the previous holes. This is necessary for taking into account the fact that previous holes are surrounded by a polymer ring that prevents the occurrence of a new hole (see Section 3.1). Such distance is progressively higher in our model, and so it is the diameter of the hole, as the number of holes increases, since the size of the hole increases as the RIE progresses. In addition, and following the same rational, the depth of the hole is higher as the RIE moves on.

We have measured a difference of 150 nm between the most and the less profound holes (see for instance Fig. 2(e)) and this is the difference that has been included in our modeling geometric sample.

The generated sample, automatically discretized into layers by Argia, is shown in Fig. 11(a). The gratings obtained of simulating 30, 60 and 120 seconds of smoothing process using CA, and discretized into 4-nm-thick layers, are shown in Fig. 12. We can observe some similarities with the experimental samples, derived from the input parameters, such as the shape, height and width of the holes, and some dissimilarities such as that the peaks are not flush with the surface and that they are sharp, instead of rounded (in contrast with what we see in the experimental sample in Fig. 2). Figure 11(b) shows an image of the layer number 100 out of the 180 layers that the sample has been discretized for the simulation, which can be compared with the SEM top-view image of the experimental RIE sample (Fig. 1).

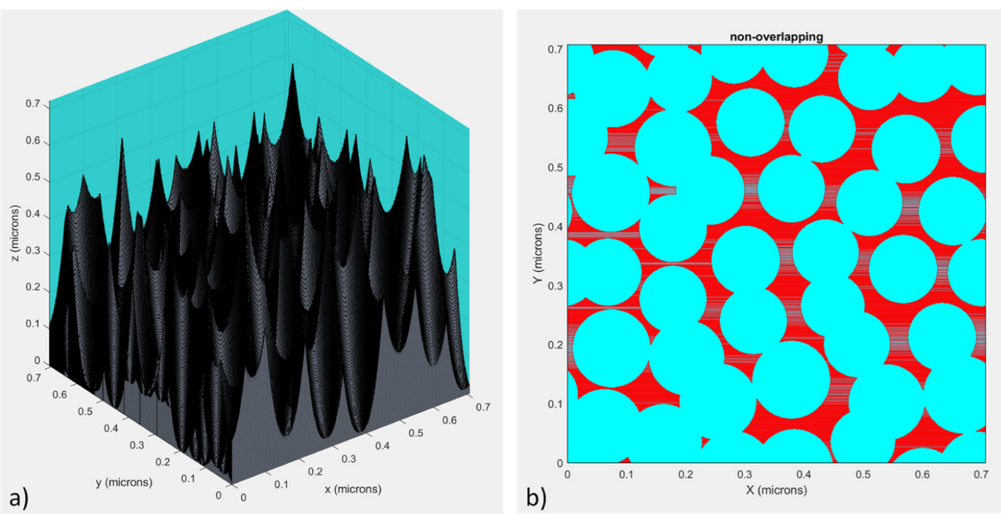

Fig. 11. a) Discretization into 180 layers of the grating after RIE; and b) layer number 100, composed of air (background in blue) and silicon (gray rectangles with red border).

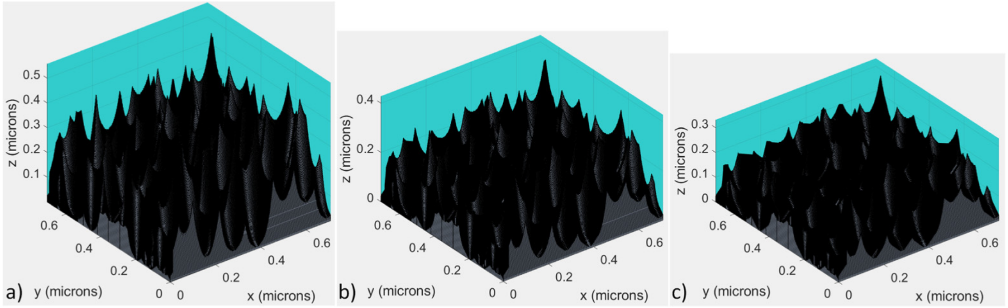

Fig. 12. a), b) and c) Discretization into 140/107/83 layers of gratings obtained simulating 30/60/120 secs of smoothing (cellular automaton, Section 4.). Layers are 4-nm-thick.

The simulated reflectance results are depicted in Fig. 13. As it was expected, the oscillations observed for the hexagonal unit cell (Fig. 8) have been significantly reduced, due to the randomization of the holes in the 0.5 μm^2 sample. This allows us to make a more direct comparison with the experimental results (Fig. 3(b)). In this sense, the specific reflectance values

Research Article Vol. 32, No. 10 / 6 May 2024 / Optics Express 17716

are in good agreement for the 120 secs smoothing sample, but not for the RIE, 30 and 60 secs samples. The reflectance of the simulated RIE curve is significantly lower that the experimental curve, and there are two reasons for this. On one hand, the height of the peaks on the modeled samples have a random distribution, which result on a smoother transition between the air and the sample compared to the experimental sample, where all the peaks have almost the same height. On the other hand, the peaks on the modeled sample are sharp, while in the experimental samples are rounded.

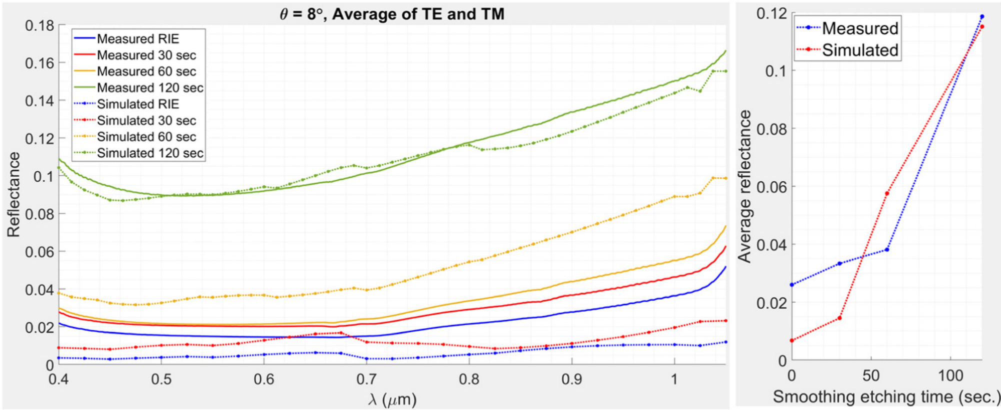

Fig. 13. Simulated reflectance of the 0.5 μm^2 gratings using Argia and experimental data from Fig. 3(b).

6.3. Rounding effect

The grating considered in the previous section reproduces neither the rounding profile that is observed for the peaks in Fig. 2, nor the effect that all the peaks are almost aligned to the same height. Both effects can be explained in terms of the sidewall that becomes tougher to remove when two holes interact each other, and even more when three or more holes interact each other.

In order of taking these effects into account, we have generated a new modeled RIE sample, where the shape of the holes has been modified, by curve fitting, to include the rounding effect observed in the experimental samples. With this new RIE sample, we have used the cellular automaton for several smoothing times, and then we simulated the reflectance for three different

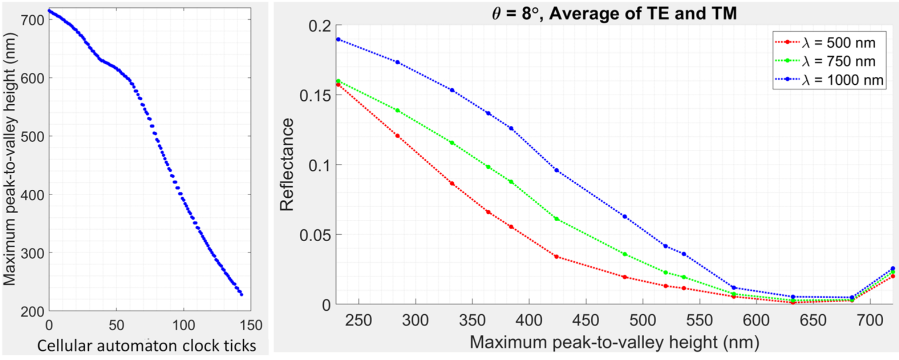

Fig. 14. Maximum peak-to-valley height, and reflectance as smoothing progresses.

Optics EXPRESS

wavelengths (see Fig. 14): 500, 750 and 1000 nm. We can observe that the reflectance is higher at the initial sample, where the total height is 720 nm, than after applying the smoothing where the total height of the sample is more than 200 nm lower. This is explained by two effects. The smoothing gradually removes the rounding, so that the increase in reflectance due to a reduction in the total height is compensated by the peak sharping effect. The other compensating effect is the gradual thinning of the peaks. In this way, the behavior observed in experimental samples – i.e., the smoothing process being capable of reducing the total height of the sample, while keeping the reflectance low – has been reproduced and explained using modeling and simulation.

7. Conclusion

We have prepared and characterized several samples using industry relevant processes: RIE and chemical smoothing. A new approach has been developed to reproduce the surface geometry and the resulting reflectance. This is new in the sense that the modeling tools (geometric model for RIE, and cellular automaton for the smoothing) are based on the real process behavior, and the resulting surface geometry and its reflectance can be related to process parameters.

The main results are: a reasonably good understanding of the geometric features of the black silicon resulting after the RIE texturing process and after the smoothing chemical etch; a good matching of the experimental results using a very simple and efficient (in terms of reflectance simulation runtime) hexagonal unit cell; and finally a better agreement with the experimental results when using a generated 0.5 square microns sample. The results show that the average reflectances below 6% can be achieved for structures with peak-to-valley heights ranging from 716 nm to 360 nm, and that this can be achieved by using reactive ion etching (RIE) followed by an isotropic chemical etching for the smoothing of between 0 and 60 seconds, which is applicable to a relevant industry sector (solar cell manufacturing), and other relevant materials and devices such as photodetectors and optical devices in general requiring low coupling losses. The nanopore diameter increases with the smoothing, sharpening the peaks and lowering the reflectances.

Funding. Universidad Nacional de Educación a Distancia (Ayudas para publicar en acceso abierto UNED 2023, Convocatoria Proyectos de Investigacion UNED 2022); Ministerio de Ciencia e Innovación (APPI, CHEER-UP, Ref. JTC-2-2019-30, ICTS-2017-28-UPV-9).

Acknowledgments. Special acknowledgments to Dr. Pierre Saint-Cast (from Fraunhofer Institute for Solar Energy Systems ISE) and Eduardo Fornies (formerly at Aurinka Photovoltaic Group) for his encouraging support of the developments of this work.

Disclosures. The authors declare no conflicts of interest.

Data availability. Data underlying the results presented in this paper are not publicly available at this time but may be obtained from the authors upon reasonable request.

References

1. "Solar (photovoltaic) panel prices vs. cumulative capacity," (2023). https://archive.ph/hHJOR [Accessed: 2023/11/29].
2. A. Fell and P. Altermatt, "A detailed full-cell model of a 2018 commercial PERC solar cell in Quokka3," IEEE J. Photovoltaics **8**(6), 1443–1448 (2018).
3. S. Zhong, Z. Huang, X. Lin, *et al.*, "High-efficiency nanostructured silicon solar cells on a large scale realized through the suppression of recombination channels," Adv. Mater. **27**(3), 555–561 (2015).
4. J. Oh, H.-C. Yuan, and H. M. Branz, "An 18.2%-efficient black-silicon solar cell achieved through control of carrier recombination in nanostructures," Nat. Nanotechnol. **7**(11), 743–748 (2012).
5. M. A. Green, *Solar Cells: Operating Principles, Technology and System Applications* (Prentice-Hall, 1982).
6. U. Gangopadhyay, S. Dhungel, P. Basu, *et al.*, "Comparative study of different approaches of multicrystalline silicon texturing for solar cell fabrication," Sol. Energy Mater. Sol. Cells **91**(4), 285–289 (2007).
7. K. Kim, S. Dhungel, S. Jung, *et al.*, "Texturing of large area multi-crystalline silicon wafers through different chemical approaches for solar cell fabrication," Sol. Energy Mater. Sol. Cells **92**(8), 960–968 (2008).
8. B. Meinel, T. Koschwitz, C. Blocks, *et al.*, "Comparison of diamond wire cut and silicon carbide slurry processed silicon wafer surfaces after acidic texturisation," Mater. Sci. Semicond. Process. **26**, 93–100 (2014).
9. M. Lippold, F. Buchholz, C. Gondek, *et al.*, "Texturing of SiC-slurry and diamond wire sawn silicon wafers by HF-HNO_3-H_2SO_4 mixtures," Sol. Energy Mater. Sol. Cells **127**, 104–110 (2014).

Optics EXPRESS

10. S. C. Baker-Finch, K. R. McIntosh, and M. L. Terry, "Isotextured silicon solar cell analysis and modeling 1: Optics," IEEE J. Photovoltaics **2**(4), 457–464 (2012).
11. X. Liu, P. R. Coxon, M. Peters, *et al.*, "Black silicon: fabrication methods, properties and solar energy applications," Energy Environ. Sci. **7**(10), 3223–3263 (2014).
12. A. Richter, R. Müller, J. Benick, *et al.*, "Design rules for high-efficiency both-sides-contacted silicon solar cells with balanced charge carrier transport and recombination losses," Nat. Energy **6**(4), 429–438 (2021).
13. S. Wang, T. Xie, R. Liang, *et al.*, "An artificial-intelligence-assisted investigation on the potential of black silicon nanotextures for silicon solar cells," ACS Appl. Nano Mater. **5**(8), 11636–11647 (2022).
14. VDMA, *International roadmap for photovoltaic, ITRPV* (VDMA, 2020).
15. P. Zheng, J. Xu, H. Sun, *et al.*, "21.63% industrial screen-printed multicrystalline Si solar cell," Phys. Status Solidi RRL **11**(3), 1600453 (2017).
16. S. Zhang, Y. Yang, D. Chen, *et al.*, "19.86% aperture efficient world record P-type multi-crystalline module with 20.59% efficient PERC solar cells," in *Proc. 44th IEEE Photovolt. Spec. Conf*, (2017).
17. T. H. Fung, T. P. Pasanen, Y. Zhang, *et al.*, "Improved emitter performance of RIE black silicon through the application of in-situ oxidation during $POCl_3$ diffusion," Sol. Energy Mater. Sol. Cells **210**, 110480 (2020).
18. B. Kafle, T. Freund, S. Werner, *et al.*, "On the nature of emitter diffusion and screen-printing contact formation on nanostructured silicon surfaces," IEEE J. Photovoltaics **7**(1), 136–143 (2017).
19. B. Kafle, T. Freund, A. Mannan, *et al.*, "Plasma-free dry-chemical texturing process for high-efficiency multicrystalline silicon solar cells," Energy Procedia **92**, 359–368 (2016). Proceedings of the 6th International Conference on Crystalline Silicon Photovoltaics.
20. CAS140CT, *Instrument Systems CAS 140CT, User manual* (Instrument Systems GmhH, 2007).
21. J. Rentsch, B. Kafle, M. Hofmann, *et al.*, "Texture etching technologies for diamond-wire-sawn mc-Si solar cells," Photovoltaics International **38** (2018).
22. N. Tucher, H. T. Gebrewold, and B. Bläsi, "Field stitching approach for the wave optical modeling of black silicon structures," Opt. Express **26**(22), A937–A945 (2018).
23. Y. Wang, B. Shao, Z. Zhang, *et al.*, "Broadband and omnidirectional antireflection of Si nanocone structures cladded by SiN film for Si thin film solar cells," Opt. Commun. **316**, 37–41 (2014).
24. S. C. Kim, "Simulation of rough surface of CIGS (CuInGaSe) solar cell by RCWA (Rigorous Coupled Wave Analysis) considering the incoherency of light," J. Opt. Soc. Korea **18**(2), 180–183 (2014).
25. A. J. Bett, J. Eisenlohr, O. Höhn, *et al.*, "Wave optical simulation of the light trapping properties of black silicon surface textures," Opt. Express **24**(6), A434–A445 (2016).
26. A. A. Elsayed, Y. M. Sabry, F. Marty, *et al.*, "Optical modeling of black silicon using an effective medium/multi-layer approach," Opt. Express **26**(10), 13443–13460 (2018).
27. S. Ma, S. Liu, Q. Xu, *et al.*, "A theoretical study on the optical properties of black silicon," AIP Adv. **8**(3), 035010 (2018).
28. N. Ravindra, "Modeling of optical properties of black silicon/crystalline silicon," Journal of Scientific and Industrial Metrology **1**, 1–7 (2015).
29. X. Li, Z. Gao, D. Zhang, *et al.*, "High-efficiency multi-crystalline black silicon solar cells achieved by additive assisted Ag-MACE," Sol. Energy **195**, 176–184 (2020).
30. Y. C. Lee, S. C. Tseng, H. L. Chen, *et al.*, "Using autocloning effects to develop broad-bandwidth, omnidirectional antireflection structures for silicon solar cells," Opt. Express **18**(S3), A421–A431 (2010).
31. A. Mavrokefalos, S. E. Han, S. Yerci, *et al.*, "Efficient light trapping in inverted nanopyramid thin crystalline silicon membranes for solar cell applications," Nano Lett. **12**(6), 2792–2796 (2012).
32. W.-L. Min, B. Jiang, and P. Jiang, "Bioinspired self-cleaning antireflection coatings," Adv. Mater. **20**(20), 3914–3918 (2008).
33. R. Rumpf, "Design and optimization of nano-optical elements by coupling fabrication to optical behavior," Ph.D. thesis, College of Optics and Photonics, University of Central Florida, USA (2006).
34. M. Auer, "Numerical treatment of localized fields in rigorous diffraction theory and its application to light absorption in structured layers," Ph.D. thesis, The Faculty of Mathematics and Computer Science, Heidelberg University, Germany (2016).
35. L. Li, "New formulation of the Fourier modal method for crossed surface-relief gratings," J. Opt. Soc. Am. A **14**(10), 2758–2767 (1997).
36. M. G. Moharam, D. A. Pommet, E. B. Grann, *et al.*, "Stable implementation of the rigorous coupled-wave analysis for surface-relief gratings: enhanced transmittance matrix approach," J. Opt. Soc. Am. A **12**(5), 1077–1086 (1995).
37. J. P. Hugonin and P. Lalanne, "RETICOLO software for grating analysis," Institut d'Optique, Orsay, France *arXiv*, arXiv:2101.00901v3 (2023).
38. E. B. Grann, M. G. Moharam, and D. A. Pommet, "Optimal design for antireflective tapered two-dimensional subwavelength grating structures," J. Opt. Soc. Am. A **12**(2), 333–339 (1995).
39. K. Han and C.-H. Chang, "Numerical modeling of sub-wavelength anti-reflective structures for solar module applications," Nanomaterials **4**(1), 87–128 (2014).

158.42.234.76 {ts '2024-07-24 05:41:13'}